Development Length and Transport Regimes of Buoyant Plastics in Open-Channel Flows

Charuni Wickramarachchi[1], Felipe Condo[1], Robert K. Niven[1,2], and Matthias Kramer[1]

[1]University of New South Wales, School of Engineering and Technology (SET), Canberra, ACT 2610, Australia
[2]Auckland University of Technology, School of Engineering, Computer and Mathematical Sciences, Auckland, New Zealand

Key Points:

- A first-passage formulation defines a particle development length for buoyant plastics in open-channel flows
- Surface tension effects may limit the applicability of the Rouse profile to positively buoyant plastics
- A Surface Detachment–Rouse chart delineates transport regimes for both positively and negatively buoyant plastics

Corresponding author: Matthias Kramer, m.kramer@unsw.edu.au

Abstract
Recent studies suggest that the vertical distribution of positively buoyant plastic particles in turbulent open-channel flows can be described by a modified Rouse profile. However, experimental evidence also indicates that floating particles often remain confined to the air–water interface due to surface tension, with limited vertical exchange. These observations suggest a tension in the interpretation of Rouse-type profiles for positively buoyant plastics. To address this, we first derive an expression for a particle development length, defined as the streamwise distance required for particles to interact with the controlling boundary. This provides a diagnostic measure of whether particles have had sufficient opportunity to interact with the boundary, and suggests that previous experimental studies may have operated within a developing regime. Second, we develop a regime map that integrates free-surface detachment and bed-entrainment processes within the Rouse framework, providing a predictive description of when Rouse-type behaviour is physically valid for both positively and negatively buoyant plastics. Together, these results highlight the critical role of boundary interactions in plastic transport and support improved prediction of plastic pollution dynamics in riverine environments.

1 Introduction

The distribution and behaviour of plastic particles in aquatic environments have become crucial areas of research due to the widespread issue of plastic pollution. A key question in understanding plastic transport and distribution in riverine systems is whether negatively and positively buoyant plastics follow traditional sediment transport models, such as the Rouse equation.

The Rouse equation provides a theoretical solution to the advection-diffusion equation for sediment transport in water and has been widely used to estimate the vertical distribution of suspended sediment concentrations (Rouse, 1937). The resulting Rouse profile is based on several key assumptions: (i) the flow is two-dimensional, steady, and uniform, with the streamwise velocity representing the dominant flow direction; (ii) the time-averaged vertical velocity is zero, although instantaneous vertical fluctuations are nonzero; and (iii) suspended particles are diffusively transported from regions of high to low concentration until equilibrium is achieved between the downward flux due to gravitational settling (deposition) and the upward flux due to turbulent diffusion (entrainment) (Dey, 2014).

Since the Rouse equation was developed to describe the behaviour of suspended sediment, it implicitly assumes that particles are denser than water. This allows for interaction between settling particles and the bed boundary, with continuous exchange between the bed load and suspended load under equilibrium conditions. Such exchange is facilitated by lift forces capable of re-entraining settled particles into the flow. In contrast, plastic densities typically range between 850 and 1410 kg/m^3 (Gent et al., 2009; Mark, 2009; Grigorescu et al., 2019), meaning that plastic particles can be either positively or negatively buoyant. Cowger et al. (2021) were among the first to demonstrate that the classical Rouse formulation can be extended to positively buoyant particles, leading to an inversion of the concentration profile and accumulation toward the free surface. This extension can be expressed within the classical Rouse framework as

$$\frac{\overline{c}}{\overline{c}_{\mathrm{ref}}} = \left(\frac{\frac{H}{z_{\mathrm{ref}}} - 1}{\frac{H}{z} - 1} \right)^{\beta_p}, \tag{1}$$

where $\overline{c}$ is the particle concentration, $\overline{c}_{\mathrm{ref}}$ is a reference concentration, H is the water depth, z_{ref} is the reference elevation, and z is the vertical coordinate. The Rouse number is defined as

$$\beta_p = \frac{w_s}{\kappa u_*}, \tag{2}$$

where w_s is the particle settling velocity (taken as positive downward), u_* is the shear velocity, and κ is the von Kármán constant. With this convention, negatively buoyant (settling) particles correspond to $\beta_p > 0$, recovering the classical sediment case. Positively buoyant (rising) particles are described by $\beta_p < 0$, leading to an inversion of the concentration profile and accumulation toward the free surface. Note that the derivation of Equation (1) assumes a parabolic eddy-viscosity profile and a turbulent Schmidt number of unity (i.e., equal turbulent diffusivities for momentum and mass), consistent with the formulation adopted by Cowger et al. (2021) and Valero et al. (2022) for buoyant litter transport.

Figure 1 illustrates an example application of Equation 1 for both positively and negatively buoyant plastic particles, where the reference level for the surface layer was set to $z_{\mathrm{ref,surf}}/H = 0.95$, and for the bed layer to $z_{\mathrm{ref,bed}}/H = 0.05$.

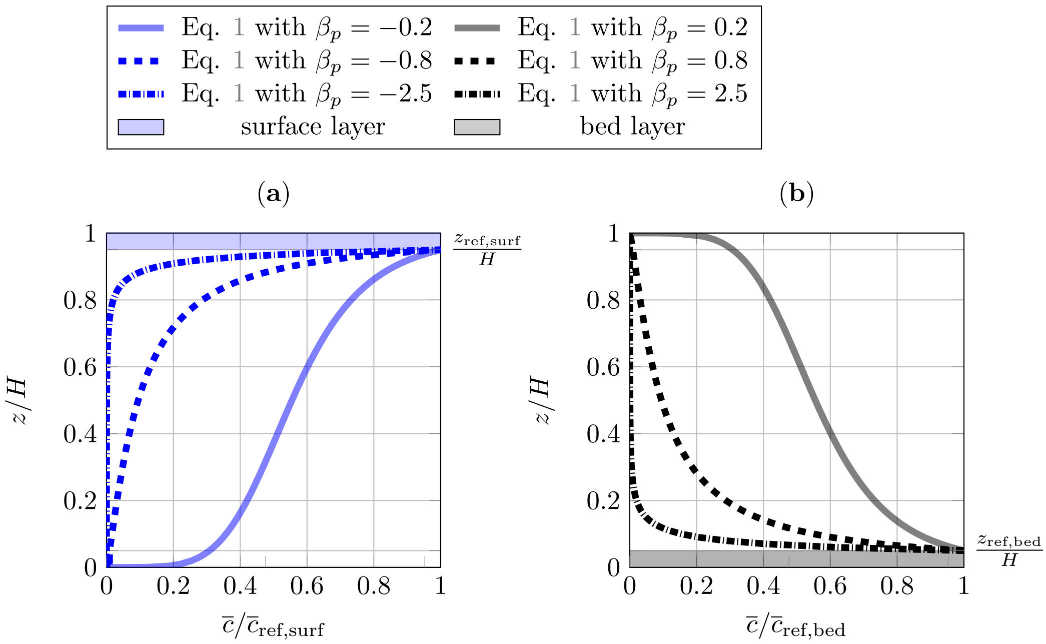

Figure 1. Modified Rouse profile for (**a**) positively buoyant plastic particles with a reference level $z_{\mathrm{ref,surf}}/H = 0.95$; (**b**) negatively buoyant plastic particles with a reference level $z_{\mathrm{ref,bed}}/H = 0.05$

Equation 1 has been applied in several studies to characterize the vertical distribution of positively buoyant plastics, including Cowger et al. (2021) and Wright et al. (2022). While these studies indicate the applicability of the Rouse framework to buoyant particles, they do not account for surface tension forces, which can entrap particles at the air–water interface and inhibit exchange between the surface layer and the underlying flow. This mechanism has been highlighted in recent studies, including Valero et al. (2022) and Kramer (2025), suggesting that surface retention may play a dominant role in the transport of buoyant particles.

Further, several experimental studies in the literature report Rouse-type concentration profiles for buoyant plastics, yet simultaneously observe that floating particles remain confined to the free surface, even under turbulent conditions. This inconsistency remains unresolved. For example, Alsina et al. (2020) released floating particles at the free surface of a wave tank and observed that "*within the experimental conditions, floating particles do not detach from the free surface, showing a large influence of the particle positive buoyancy*". Similarly, Zaat (2020) performed flume experiments with HDPE sheets and reported that "*releasing of plastic at the water surface did not result in mixing at all. Sheets would remain at the* *surface due to surface tension*". Finally, Born et al. (2023) observed in an open-channel flume that floating particles "*remained at the water surface, even under intense inlet turbulence caused by the discharge entering the flume from the pump*".

Taken together, these observations suggest a tension in the interpretation of Rouse-type profiles for positively buoyant plastics. While Rouse-like concentration distributions have been reported, experimental evidence also indicates that floating particles can remain confined to the free surface, with limited vertical exchange. This is critical because the Rouse formulation assumes an equilibrium established through interaction with the controlling boundary. If particles are retained at the surface by surface tension, or have not travelled sufficiently far to interact with that boundary, the resulting concentration profile may not represent a true equilibrium state.

This motivates two hypotheses. First:

"*If a boundary exerts a controlling influence on particle distributions, a representative concentration profile is only established after particles have travelled a finite development length sufficient to enable interaction and exchange with that boundary.*"

The second is:

"*A Rouse profile can only exist for positively buoyant plastics when particle–surface interactions sustain vertical exchange, which requires detachment from the free surface rather than surface-tension-driven retention.*"

To test these hypotheses, we adopt a combined analytical and numerical approach. First, we derive an analytical expression for a particle development length based on a first-passage formulation (§ 2), representing the streamwise distance required for particles to reach and interact with the governing boundary. This provides a quantitative measure of the distance over which boundary-controlled processes can influence particle distributions. Second, we perform Lagrangian transport simulations of an idealized two-dimensional open-channel flow (§ 3) under controlled turbulence conditions. To represent surface entrapment, we implement an absorbing surface boundary condition, whereby particles are irreversibly captured at the free surface. This formulation enables direct comparison between the first-passage framework and Lagrangian simulations, providing a basis for validating the analytical predictions. Finally, we compare the particle development lengths with experimental studies from the literature (§ 4) and develop a regime map delineating the conditions under which the Rouse profile is expected to hold for both positively and negatively buoyant plastics (§ 5).

2 Particle Development Length

2.1 Vertical first-passage formulation

The particle development length can be formulated as a first-passage problem by treating the particle elevation as a stochastic process subject to upward buoyant drift and turbulent vertical diffusion. In this framework, the relevant quantity is the downstream distance associated with the time required for a particle released below the free surface to first reach a thin near-surface capture layer. Let the particle be released at the dimensionless elevation

$$\zeta = \frac{z_{\text{source}}}{H}, \tag{3}$$

where z_{source} is the vertical release position measured from the bed and H is the local water depth. We introduce the dimensionless vertical coordinate

$$\eta = \frac{z}{H}, \tag{4}$$

where z is measured upward from the bed. Surface arrival is then defined as the first passage to a thin capture layer located at $\eta = 1 - \varepsilon$, where $\varepsilon \ll 1$. The capture layer thickness is taken to correspond to a characteristic particle size D_p, such that $\varepsilon = (\frac{1}{2}\, D_p)/H$.

Assuming steady, uniform, unidirectional flow, the vertical particle motion is represented as an advection–diffusion process with constant upward rise velocity and turbulent diffusivity following the parabolic profile commonly used in open-channel flow (Nezu & Nakagawa, 1993)

$$\mathcal{D}_z(z) = \kappa u_* z \left(1 - \frac{z}{H}\right), \tag{5}$$

where u_* is the shear velocity and $\kappa = 0.41$ is the von Kármán constant. The corresponding streamwise velocity is described using a logarithmic profile (Dey, 2014)

$$u(z) = \frac{u_*}{\kappa} \ln\left(\frac{z}{z_0}\right), \tag{6}$$

where z_0 is the hydraulic roughness length. This profile is used to relate the first-passage time to the downstream particle development length.

Let $T(z)$ denote the mean first-passage time for a particle starting at elevation z to reach the near-surface layer $(1-\varepsilon)H$. The quantity of interest is therefore $T(z_{\text{source}})$, corresponding to a particle released at $z = z_{\text{source}}$. Following Gardiner (1985), the backward Kolmogorov equation governing T is

$$\mathcal{D}_z(z)\,\frac{\mathrm{d}^2 T}{\mathrm{d}z^2} + \left(\frac{\mathrm{d}\mathcal{D}_z}{\mathrm{d}z} - w_s\right)\frac{\mathrm{d}T}{\mathrm{d}z} = -1, \tag{7}$$

where w_s is the settling velocity, taken as positive downward. For positively buoyant particles, $w_s < 0$, such that $-w_s$ represents the upward rise velocity. The boundary conditions are

$$\frac{\mathrm{d}T}{\mathrm{d}z}(0) = 0, \qquad T\big((1-\varepsilon)H\big) = 0. \tag{8}$$

Introducing the dimensionless mean first-passage time

$$\Phi(\eta) = \frac{\kappa u_*}{H}\,T(\eta H), \tag{9}$$

and the Rouse number $\beta_p = w_s/(\kappa u_*)$, Equation (7) becomes

$$\eta(1-\eta)\,\frac{\mathrm{d}^2\Phi}{\mathrm{d}\eta^2} + \big(1 - 2\eta - \beta_p\big)\,\frac{\mathrm{d}\Phi}{\mathrm{d}\eta} = -1, \tag{10}$$

with boundary conditions

$$\frac{\mathrm{d}\Phi}{\mathrm{d}\eta}(0) = 0, \qquad \Phi(1-\varepsilon) = 0. \tag{11}$$

The quantity $\Phi(\zeta)$ therefore represents the dimensionless mean first-passage time required for a particle released at $z = z_{\text{source}}$ to first reach the near-surface layer. Equation (10) does not generally admit a simple elementary solution, but it can be written in integral form and solved efficiently numerically. Its limiting behaviour is, however, obtained analytically, yielding distinct turbulence-driven and buoyancy-driven asymptotic scalings.

2.2 Asymptotic regimes

To convert this first-passage time into a development length, we introduce a representative horizontal advection velocity scale U. The corresponding dimensionless development length is then

$$\frac{L}{H} = \frac{U}{\kappa u_*}\,\Phi(\zeta). \tag{12}$$

For positively buoyant particles, $\beta_p < 0$, and $-\beta_p$ represents the relative strength of upward buoyant transport to turbulent mixing. Two asymptotic regimes follow directly from Equation (10). For $-\beta_p \ll 1$, vertical transport is turbulence-driven, and the mean first-passage solution scales as (Appendix A)

$$\Phi(\zeta) \sim \ln\left(\frac{1-\zeta}{\varepsilon}\right), \qquad -\beta_p \ll 1. \tag{13}$$

Hence,

$$\frac{L}{H} \sim \frac{U}{\kappa u_*} \ln\left(\frac{1-\zeta}{\varepsilon}\right), \qquad -\beta_p \ll 1. \tag{14}$$

For $-\beta_p \gg 1$, vertical transport is buoyancy-driven, and the mean first-passage solution scales as (Appendix A)

$$\Phi(\zeta) \sim \frac{1-\zeta-\varepsilon}{-\beta_p}, \qquad -\beta_p \gg 1. \tag{15}$$

Thus,

$$\frac{L}{H} \sim \frac{U}{\kappa u_*}\left(\frac{1-\zeta-\varepsilon}{-\beta_p}\right) = \frac{U\,(1-\zeta-\varepsilon)}{-w_s}, \qquad -\beta_p \gg 1. \tag{16}$$

Equations (14) and (16) define two physically distinct limits of the particle development length. In the turbulence-driven limit ($-\beta_p \ll 1$), vertical transport is controlled by diffusion, and the logarithmic dependence on $(1-\zeta)/\varepsilon$ reflects the time required for a particle to diffuse across the depth to the surface. In the buoyancy-driven limit ($-\beta_p \gg 1$), the development length reduces to the distance for ballistic rise across the depth multiplied by the mean flow velocity, recovering the scaling $L \sim UH/(-w_s)$.

Notably, the same scaling emerges in Claudin et al. (2011), who identified it as the relaxation length governing the downstream distance required for a suspended sediment flux to reach equilibrium following a change in flow conditions. The emergence of this behaviour within the present framework suggests that particle development lengths for buoyant plastics belong to the broader class of relaxation phenomena governing turbulent suspensions.

2.3 Horizontal velocity closure

To obtain an explicit hydraulic expression for the particle development length, the representative horizontal advection velocity U may be approximated by the depth-averaged streamwise velocity above the release elevation,

$$U = \frac{1}{(1-\zeta)H}\int_{\zeta H}^{H} \overline{u}(z)\,\mathrm{d}z. \tag{17}$$

Assuming that the streamwise velocity follows the logarithmic law, Equation (6), one obtains

$$\frac{U}{\kappa u_*} = \frac{1}{\kappa^2(1-\zeta)}\left[\ln\left(\frac{H}{z_0}\right) - \zeta\ln\left(\frac{\zeta H}{z_0}\right) - (1-\zeta)\right]. \tag{18}$$

The two asymptotic limits for the development length may therefore be written explicitly as

$$\frac{L}{H} \sim \frac{\ln\left(\frac{1-\zeta}{\varepsilon}\right)}{\kappa^2(1-\zeta)}\left[\ln\left(\frac{H}{z_0}\right) - \zeta\ln\left(\frac{\zeta H}{z_0}\right) - (1-\zeta)\right], \qquad -\beta_p \ll 1, \tag{19}$$

and

$$\frac{L}{H} \sim \frac{1-\zeta-\varepsilon}{\kappa^2(-\beta_p)(1-\zeta)}\left[\ln\left(\frac{H}{z_0}\right) - \zeta\ln\left(\frac{\zeta H}{z_0}\right) - (1-\zeta)\right], \qquad -\beta_p \gg 1. \tag{20}$$

Physically, Equations (19) and (20) show that the development length increases as $-\beta_p$ decreases, reflecting situations where the upward rise velocity weakens or turbulent mixing dominates. The effect of bed roughness enters through z_0, which shapes the velocity profile and thus the horizontal transport of the particle. Particles released deeper in the flow (smaller ζ) have farther to rise and are transported farther downstream.

The impact of these processes on the particle development lengths is illustrated in Figure 2**a**, which shows the general solution of Equation (10) via Equation (12) together with the two asymptotic limits. At large $-\beta_p$, the buoyancy-driven scaling provides a close approximation to the general solution, while at small $-\beta_p$ the diffusion-dominated scaling governs. Equating Equations (19) and (20) gives the transition between both regimes at

$$-\beta_p^* \sim \frac{1-\zeta-\varepsilon}{\ln\left(\frac{1-\zeta}{\varepsilon}\right)}, \tag{21}$$

which evaluates to $-\beta_p^* \approx 0.2$ for the parameters used in Figure 2**a**. Notably, this transition occurs well below the classical criterion $|\beta_p| = 1$ for physically relevant combinations of ε and ζ (Figure 2**b**), reflecting the amplifying effect of the logarithmic factor in the diffusion-dominated limit. It is important to note, however, that $-\beta_p^*$ does not represent the classical transition between suspended and buoyancy-dominated transport in the Rouse sense. Rather, it defines the crossover between diffusion-controlled and buoyancy-controlled scaling of the particle development length.

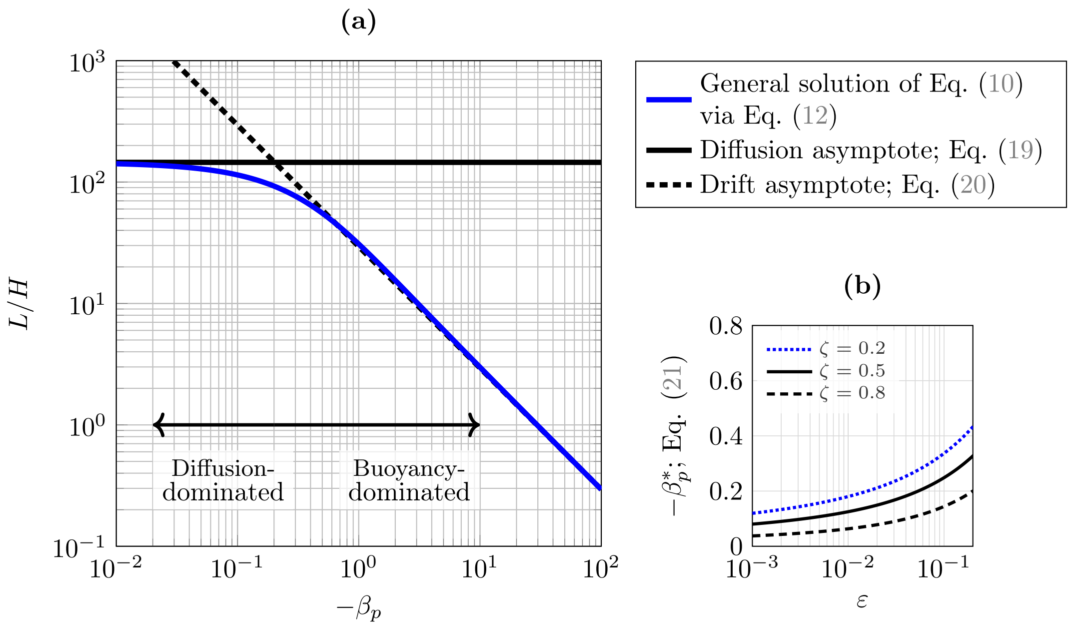

Figure 2. Particle development lengths for buoyant plastics evaluated for $H/z_0 = 1000$: (**a**) Dimensionless development length L/H as a function of $-\beta_p$ for $\zeta = 0.2$ and $\varepsilon = 1/60$; (**b**) Transition Rouse number $-\beta_p^*$ as a function of the dimensionless capture layer thickness ε for three release positions ζ.

3 Lagrangian Transport Simulations

We simulate the transport of positively buoyant plastic spheres within a two-dimensional open channel flume using a Random Walk Model. This approach extends the asymptotic solutions for the particle development length. The water depth in the simulation is $H = 0.3$ m, and the flow is described by a logarithmic velocity profile, that is, Equation (6). For the simulation, we used $u_* = 0.021$ m/s, and $z_0 = 3 \cdot 10^{-4}$ m, corresponding to a hydraulically rough bed with $H/z_0 = 1000$. These parameters resulted in a depth-averaged mean velocity of $\frac{1}{H}\int_{z=0}^{H} \overline{u}\,\mathrm{d}z = 0.3$ m/s. The selected conditions closely match those used in previous laboratory studies, enabling direct comparison and validation of our numerical results.

Particle motion is governed by its position vector $\mathbf{x}_p$, with the particle velocity defined by the time derivative

$$\frac{\mathrm{d}\mathbf{x}_p}{\mathrm{d}t} = \mathbf{u}_p, \tag{22}$$

where t denotes the time, the subscript p refers to a plastic particle, and $\mathbf{u}_p$ is the velocity vector of the point particle relative to an inertial frame of reference. Equation (22) can be reformulated using a Random Walk Model. We adopt the scheme proposed by Visser (1997), which has been successfully applied in previous studies (Nordam et al., 2019, 2023; Wickramarachchi et al., 2024). This model accounts for both advective and diffusive transport, described as follows

$$x_p(t+\Delta t) = x_p(t) \;+\; \overbrace{\overline{u}\,\Delta t}^{\text{advection step}} \;+\; \overbrace{\frac{\partial \mathcal{D}_x}{\partial x}\Delta t + \mathcal{R}\sqrt{2\Delta t \mathcal{D}_x^*}}^{\text{diffusion step}}, \tag{23}$$

$$z_p'(t+\Delta t) = z_p(t) + (\overline{w} - w_s)\Delta t + \frac{\partial \mathcal{D}_z}{\partial z}\Delta t + \mathcal{R}\sqrt{2\Delta t \mathcal{D}_z^*}. \tag{24}$$

In these expressions, x_p and z_p represent the horizontal and vertical components of the particle position vector $\mathbf{x}_p$. The superscript $'$ in Equation (24) indicates an intermediate step that is subsequently corrected to satisfy boundary conditions (e.g., particle reflection at the bed or absorption at the free surface). The time step is denoted by Δt. The terms $\overline{u}$ and $\overline{w}$ correspond to the time-averaged advection velocities in the horizontal and vertical directions, respectively, with vertical flow velocities neglected in this model ($\overline{w} \approx 0$). The turbulent diffusivities in the horizontal and vertical directions are denoted by $\mathcal{D}_x$ and $\mathcal{D}_z$, where for simplicity, we assume $\mathcal{D}_x \approx 0$, and $\mathcal{D}_z$ follows Equation (5).

The terms $\mathcal{D}_x^*$ and $\mathcal{D}_z^*$ are the local diffusivities evaluated at intermediate positions, defined as $x^* = x_p + \frac{\partial \mathcal{D}_x}{\partial x}\frac{\Delta t}{2}$ and $z^* = z_p + \frac{\partial \mathcal{D}_z}{\partial z}\frac{\Delta t}{2}$. Here, $\frac{\partial \mathcal{D}_x}{\partial x} \approx 0$, and $\frac{\partial \mathcal{D}_z}{\partial z} = \kappa u_* \left(1 - \frac{2z}{H}\right)$. The parameter $\mathcal{R}$ is a normally distributed random number with zero mean and unit standard deviation, and w_s is the terminal settling velocity of the positively buoyant plastic (negative sign). These velocities are selected so that the modified Rouse number $\beta_p = w_s/(\kappa u_*)$ takes values ranging from $-\beta_p = 0.01$ to $-\beta_p = 100$. Note that this approach does not necessarily require the selection of a particle diameter. However, as an example, assuming a plastic density of $\rho_p = 950$ kg/m^3 and applying the settling velocity formulation of Ferguson and Church (2004), the corresponding particle diameters range between approximately 0.4 mm $< D_p < 5.6$ mm. Both the assumed density and the resulting diameter range are consistent with the particle properties used in the experiments of Born et al. (2023).

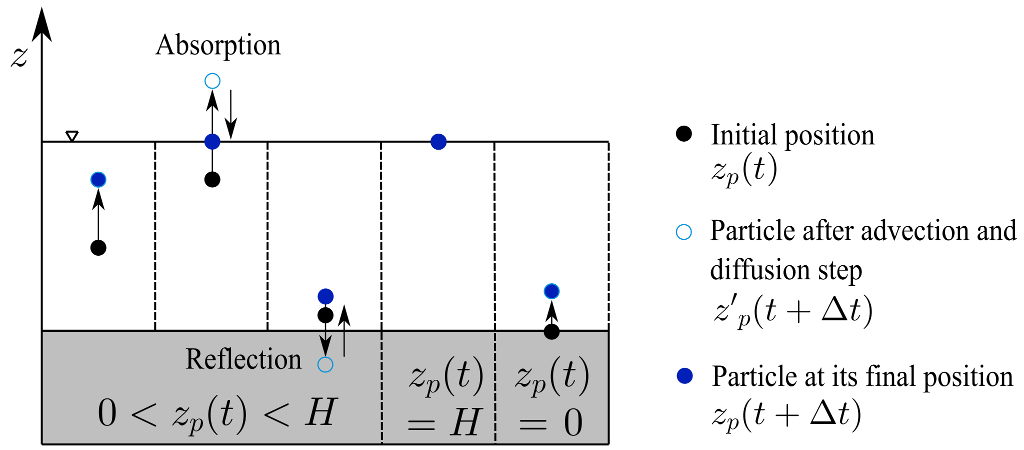

Figure 3. Illustration of implemented boundary conditions, including absorptive surface boundary and reflective bed boundary.

As the simulation domain is unbounded in the streamwise direction, boundary conditions are applied only in the vertical (z) direction, accounting for particle–bed and particle–surface interactions. Based on (i) literature evidence indicating that floating particles do not detach from the free surface under typical flow conditions (Alsina et al., 2020; Zaat, 2020; Born et al., 2023), (ii) the surface detachment formulation of Kramer (2025), which shows that the prevailing shear velocity $u_* = 0.021$ m/s falls well below the critical shear velocity required for detachment, and (iii) our own accompanying experiments demonstrating surface retention under the flow conditions considered here (Appendix B), the free surface is treated as an absorbing boundary, as exemplified in Figure 3. In contrast, the channel bed is modelled as a reflective boundary; however, interactions with the bed are rare due to the positive buoyancy of the particles. Mathematically, the boundary conditions are applied through an intermediate step, denoted as z'_p, which is subsequently corrected to ensure particles remain within the physical domain. The implementation proceeds as follows

$$z'_p(t+\Delta t) = \begin{cases} z_p(t) + (\overline{w} - w_s)\Delta t + \dfrac{\partial \mathcal{D}_z}{\partial z}\Delta t + \mathcal{R}\sqrt{2\Delta t \mathcal{D}_z^*} & \text{if } 0 < z_p(t) < H, \\ H & \text{if } z_p(t) = H, \\ \left| (\overline{w} - w_s)\Delta t + \dfrac{\partial \mathcal{D}_z}{\partial z}\Delta t + \mathcal{R}\sqrt{2\Delta t \mathcal{D}_z^*} \right| & \text{if } z_p(t) = 0. \end{cases} \tag{25}$$

$$z_p(t+\Delta t) = \begin{cases} z'_p(t+\Delta t) & \text{if } 0 \leq z'_p(t+\Delta t) \leq H, \\ H & \text{if } z'_p(t+\Delta t) > H, \quad \text{(absorptive boundary)} \\ -z'_p(t+\Delta t) & \text{if } z'_p(t+\Delta t) < 0. \quad \text{(reflective boundary)} \end{cases} \tag{26}$$

Equations (25) and (26) ensure accurate representation of particle dynamics near the boundaries, maintaining physical consistency throughout the simulation. An illustration of the implemented boundary conditions is shown in Figure 3.

4 Results

4.1 Particle Trajectories and Surface Interactions

Using the Random Walk Model as described, we performed a total of 60 simulations, comprising 20 simulations at each of the three release positions ($\zeta = 0.2$, 0.5, and 0.8). In each run, we simulated the trajectories of 100,000 positively buoyant plastic particles across a range of modified Rouse numbers logarithmically spaced from $-\beta_p = 0.01$ to $-\beta_p = 100$. The time step was $\Delta t = 0.1$ s, which is in accordance with previously established criteria (Rossman & Boulos, 1996; Gräwe et al., 2012). For each case, we tracked the length travelled by each particle before surfacing, enabling a statistical characterization of particle arrival distances.

Figure 4**a** shows exemplary trajectories of twenty particles, released at $\zeta = 0.2$, with a modified Rouse number of $-\beta_p = 5.46$. In this panel, we also added the mean arrival distance into the surface capture layer (vertical blue line), as well as the 95th percentile of the first-passage distance into the surface capture layer (vertical red line). The mean gives the streamwise distance at which a typical particle first reaches the capture layer, and the 95th percentile marks the distance within which 95 % of particles have done so.

Arrival distances follow a log-normal distribution, and their corresponding cumulative distribution function (CDF) is presented in Figure 4**b**, showing that 95 % of the particles reach the surface layer at $L_{95} \approx 2.58$ m. To connect these particle development lengths with concentration profile convergence, we next assess whether the simulated vertical distributions

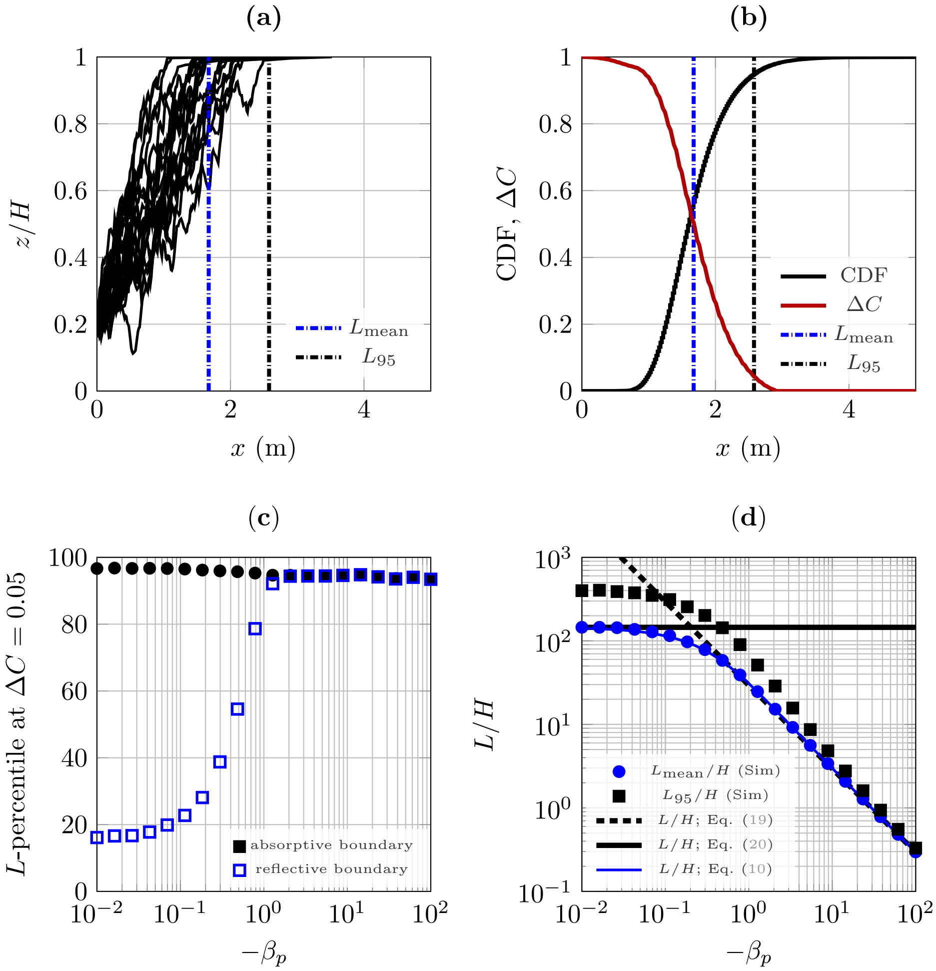

Figure 4. Numerical simulation results: (**a**) Selected trajectories of twenty particles for $-\beta_p = 5.46$, released at $\zeta = 0.2$; (**b**) Cumulative distribution function of surface arrival distances, with L_{mean} and L_{95} indicating the mean and 95th percentile of the distribution, respectively; (**c**) Percentiles of particle development lengths corresponding to the $\Delta C = 0.05$ profile-convergence criterion as a function of the modified Rouse number; (**d**) Comparison of analytical and simulated development lengths for a release position $\zeta = 0.2$; the ratio $H/z_0 = 1000$ and $\varepsilon = 1/60$ are used throughout.

attain an equilibrium downstream form. Profile convergence was quantified using the Bray-Curtis dissimilarity (Bray & Curtis, 1957)

$$\Delta C = \frac{\int_0^H |\widehat{c}_x(z) - \widehat{c}_{\mathrm{ref}}(z)|\,\mathrm{d}z}{\int_0^H (\widehat{c}_x(z) + \widehat{c}_{\mathrm{ref}}(z))\,\mathrm{d}z}, \tag{27}$$

where

$$\widehat{c}_x(z) = \frac{\overline{c}_x(z)}{\int_0^H \overline{c}_x(z)\,\mathrm{d}z} \tag{28}$$

is the local vertical concentration profile at streamwise location x, obtained by binning particle elevations over the water column and normalizing to unit area. $\widehat{c}_{\mathrm{ref}}(z)$ is the corresponding reference profile, which was taken here as the profile where 98 % of particles reached the surface, which is taken as a practical proxy for an empty water column. Note the metric ΔC is bounded between 0 and 1, where 0 indicates identical normalized profiles and 1 indicates non-overlapping profiles. ΔC is shown in Figure 4**b** as a red line, and it decreases monotonically with streamwise distance, approaching zero as the local profile converges onto the reference.

We adopt $\Delta C = 0.05$ as the convergence criterion, i.e., the streamwise location at which the local profile differs from the reference by less than 5 %, and report the corresponding percentiles of particle development lengths in Figure 4**c**. For the absorptive surface boundary, the convergence length closely tracks L_{95} across the tested range of Rouse numbers, confirming that the streamwise distance required for the vertical profile to reach its equilibrium coincides with the near-maximum particle arrival distance rather than the mean. For completeness, we also implement a reflective surface boundary, where $\widehat{c}_{\mathrm{ref}}(z)$ corresponds to the theoretical Rouse profile, representing the equilibrium state for a reflective boundary. Note that the two convergence lengths are defined relative to different reference states: for the absorptive boundary, convergence is measured relative to a fully depleted water column, whereas for the reflective boundary, it is measured relative to the Rouse equilibrium, consistent with the reflective-boundary solution of Wickramarachchi et al. (2024). For the latter, the convergence percentile increases towards $-\beta_p \approx 1$ and thereafter coincides with the absorptive convergence length (Figure 4**c**). This implies that the choice of surface boundary condition affects the development length only in the turbulence-influenced regime ($-\beta_p \lesssim 1$), where surface interaction alters the evolving profile. For $-\beta_p \gtrsim 1$, buoyant rise dominates, and both boundaries yield the same convergence length.

A comparison of the development lengths obtained from the Lagrangian transport simulations with Equations (19) and (20) is presented in Figure 4**d**. We observe a strong agreement between the analytical solutions and the simulated mean arrival distance ($L \approx L_{\mathrm{mean}}$), thereby validating the first-passage framework against the Lagrangian simulations. The development length L_{95} is significantly larger than L_{mean} (Figure 4**d**), reflecting the influence of turbulence in increasing the spread of particle arrival distances and causing some particles to travel much farther before surfacing. For practical purposes, L_{95} is more relevant than L_{mean}, since it corresponds to the streamwise distance at which the vertical concentration profile reaches convergence (Figure 4**c**). Using L_{95} as the design benchmark therefore ensures a physical domain long enough to capture the delayed arrival of turbulence-influenced particles.

While L_{mean} is approximated by L from the first-passage solution, L_{95} additionally requires the spread of the arrival-distance distribution. Because the arrival distances are log-normally distributed, the 95th percentile follows in closed form

$$\frac{L_{95}}{H} = \exp\bigl(1.645\,\sigma_L - \tfrac{1}{2}\sigma_L^2\bigr)\,\frac{L}{H}, \tag{29}$$

where 1.645 is the 95th percentile of the standard normal distribution and σ_L is the standard deviation of $\ln(L/H)$. The spread σ_L is well described by a bounded sigmoid in the modified Rouse number

$$\sigma_L = \frac{0.930}{1 + (-\beta_p/2.01)^{0.742}}, \tag{30}$$

which reproduces the simulated spread with $R^2 = 0.998$ and predicts L_{95} to within 3% on average over $0.01 \leq -\beta_p \leq 100$. The coefficients in Equation (30) are fitted for the release position $\zeta = 0.2$, which is a conservative choice; deeper releases modify the spread, since the release elevation sets the streamwise path over which turbulence acts on the rising particles. Equations (29) and (30) thus provide an explicit expression for L_{95}/H.

4.2 Comparison of Development Length with Prior Studies

Here, we compare our analytical expressions, Equation (10) via Equation (12), and Equation (29) with previous flume experiments. In Figure 5, the experimental flume lengths $(L/H)_{\mathrm{exp}}$ of Zaat (2020), Valero et al. (2022), and Born et al. (2023) are plotted on the ordinate against predicted particle development lengths L/H and L_{95}/H, which allows us to assess whether the experiments satisfied the particle development length required for profile convergence. As discussed in the previous section, L_{95} is the more relevant benchmark for practical purposes. It is seen that the majority of the experiments from Zaat (2020) and

Valero et al. (2022) may not have converged, while the experiments of Born et al. (2023) fall to the left of the 1:1 line (Figure 5**b**).

Overall, our findings suggest that several previous experiments may have been conducted within a developing regime, in which particles had not yet travelled far enough to interact with the controlling boundary, rather than under the fully developed conditions implicitly assumed by the Rouse framework. In such cases, the reported concentration profiles may reflect a transitional state rather than true equilibrium, which should be considered when interpreting the results. More constructively, the presented particle development length provides a quantitative design criterion for future experiments. Evaluating L_{95}/H from Equation (29) for the target particle and flow conditions yields a minimum flume length beyond which the vertical concentration profile is expected to have reached equilibrium. In the turbulence-dominated regime ($-\beta_p \ll 1$), however, this criterion can demand flume lengths on the order of hundreds of water depths (Figure 4**d**), which may be impractical to realise in the laboratory. This reinforces the view that equilibrium Rouse profiles are difficult to attain for weakly buoyant plastics, and that surface interactions, rather than a fully developed vertical distribution, often govern their transport.

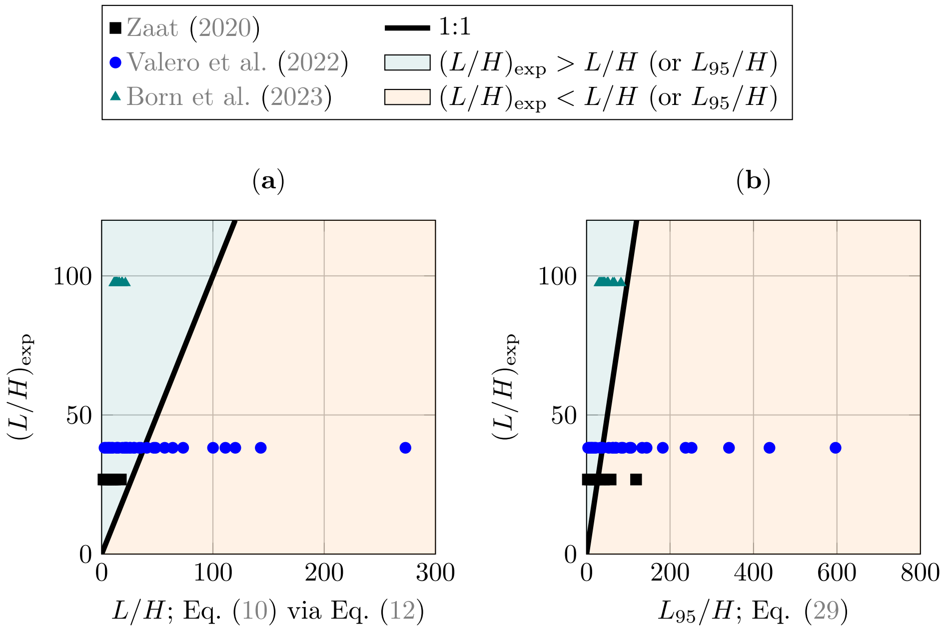

Figure 5. Comparison of particle development lengths versus previous studies: (**a**) L/H; (**b**) L_{95}/H.

5 Discussion

5.1 Surface Detachment–Rouse chart

To consolidate our study, we develop a regime map that integrates free surface detachment and bed entrainment processes with the Rouse profile. This map delineates the dominant plastic transport modes and identifies the conditions under which the Rouse profile remains valid for both positively and negatively buoyant plastics, across a range of flow regimes and particle characteristics. The regime map can be interpreted in two complementary ways: as a Surface Detachment–Rouse chart, which emphasizes surface detachment thresholds and plastic transport modes, and as a Shields–Rouse diagram, which highlights bed entrainment thresholds and transport regimes.

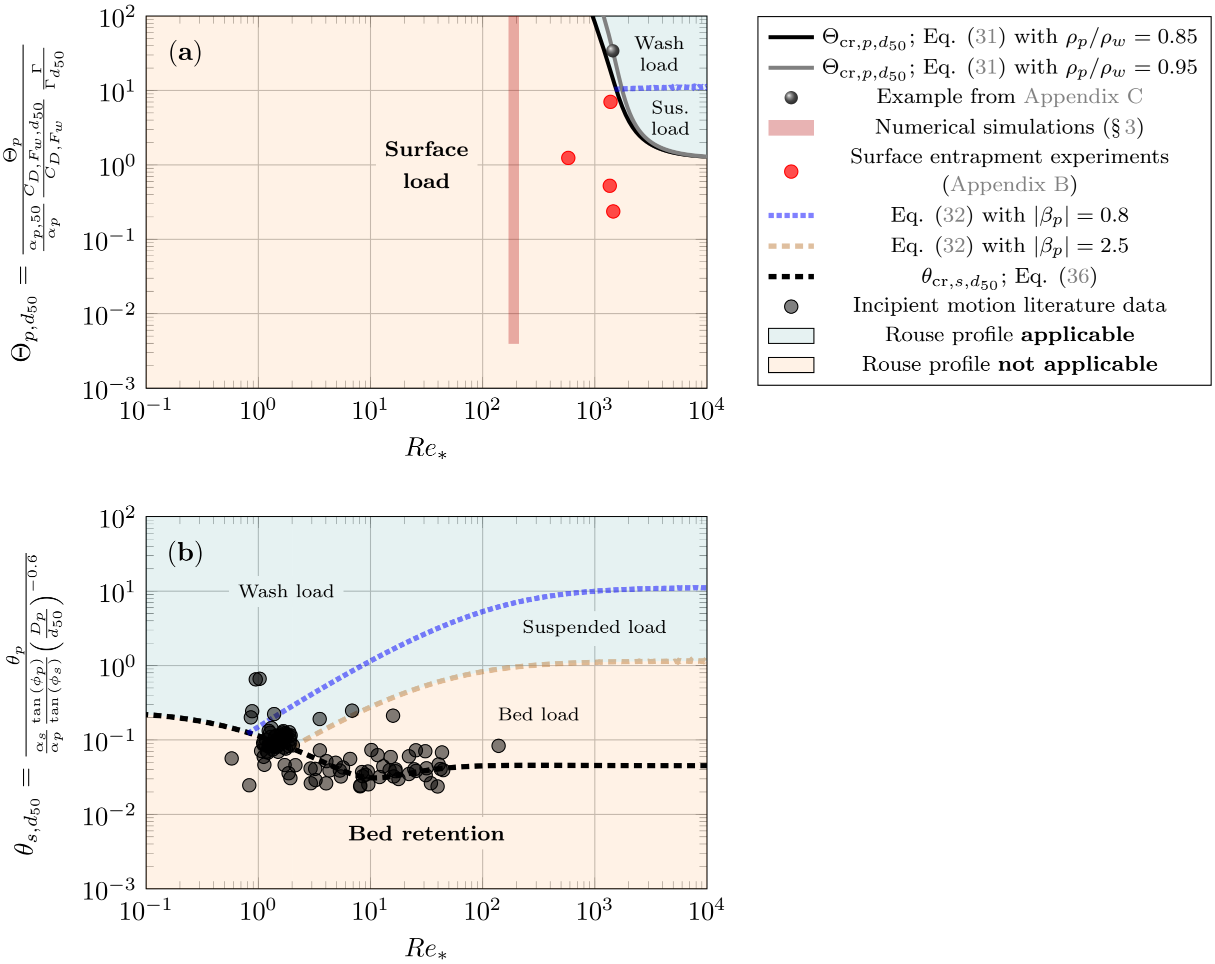

Figure 6. Regime maps for plastic transport in fluvial systems: (**a**) Surface Detachment-Rouse chart for positively buoyant plastics; the reference particle is a spherical plastic with $D_p = d_{50}$; (**b**) Shields-Rouse diagram for negatively buoyant plastics; the reference particle is a sediment particle with $D_s = d_{50}$; incipient motion literature data from Waldschläger and Schüttrumpf (2019) and Goral et al. (2023), as re-analysed by Kramer (2025).

The critical surface detachment parameter for positively buoyant plastics normalizes the critical shear velocity $u_{*,\mathrm{cr}}$ required to detach particles from the free surface against key flow and particle properties. It was first introduced by Kramer (2025), following earlier force considerations by Valero et al. (2022)

$$\Theta_{\mathrm{cr},p} = \frac{u_{*,\mathrm{cr}}^2}{\left(\frac{\rho_w - \rho_p}{\rho_w}\right) g D_p} = \frac{9.17\,\Gamma_{\mathrm{cr}}}{\alpha_p\, C_{D,F_w}}, \tag{31}$$

where $\Theta_{\mathrm{cr},p}$ is the dimensionless shear velocity at surface detachment (referred to as surface detachment parameter), and the subscript "cr" denotes a critical threshold. Here, D_p is the sphere volume-equivalent plastic diameter, g is the gravitational acceleration, ρ_w and ρ_p are the water and plastic densities, respectively. Γ_{cr} is a plastic-based Bond number at detachment (see Appendix C), and C_{D,F_w} is a drag coefficient associated with the turbulent downpull force F_w, as defined in Valero et al. (2022) and Kramer (2025). The parameter $\alpha_p = A_{\mathrm{proj}} D_p/\mathcal{V}_p$ is a shape factor, where A_{proj} is the projected area of the particle parallel to the streamwise flow direction and $\mathcal{V}_p$ is the particle volume. Note that Equation (31) is expressed in squared form compared to the original formulation in Kramer (2025), in order to align dimensionally with the classical Shields parameter. Additionally, the assumption $\rho_w > \rho_p$ implies that this formulation is specifically valid for positively buoyant plastics.

To represent Equation (31) in our Surface Detachment–Rouse chart, we first define a reference particle, analogous to how natural sediment is used in the classical Shields diagram, to normalize flow and particle properties. We select a spherical plastic particle as the reference and assume that its diameter corresponds to the median grain size of the underlying sediment, that is, $D_p = d_{50}$. This assumption maintains consistency between the two diagrams and provides a standardized basis for our analysis; the influence of varying particle shapes and sizes is addressed subsequently.

To construct the surface detachment curves, we proceed as follows: First, we select a particle size corresponding to a specified bed diameter d_{50}, as well as a particle density ρ_p. Next, we evaluate Equation (31), where the shape factor is taken as $\alpha_p = 1.5$, corresponding to a spherical particle. We also assume $C_{D,F_w} = 5$, which represents a conservative estimate for the turbulent drag coefficient acting on buoyant plastics in natural flow conditions. With these parameters, we compute $\Theta_{\mathrm{cr},p,d_{50}}$, where the subscript d_{50} indicates that this value corresponds to our reference particle. Having computed $\Theta_{\mathrm{cr},p,d_{50}}$, we evaluate the critical shear velocity using $u_{*,\mathrm{cr}} = \left(\Theta_{\mathrm{cr},p,d_{50}} \left(\frac{\rho_w - \rho_p}{\rho_w}\right) g D_p\right)^{0.5}$, which is simply a re-arrangement of Equation (31). Finally, we evaluate the shear Reynolds number as $Re_* = (u_{*,\mathrm{cr}} d_{50})/\nu_w$, where ν_w is the kinematic viscosity of water. An example calculation illustrating this procedure is provided in Appendix C and is included in Figure 6**a**.

Figure 6**a** shows the surface detachment curves for two density ratios, $\rho_p/\rho_w = 0.85$ and 0.95, representative of commercially available positively buoyant plastics. Because the normalization follows the classical Shields formulation, the density ratio enters both sides of Equation (31), leaving a residual dependence on ρ_p/ρ_w; this dependence is weak, as illustrated in Figure 6**a**. The key result is that the vast majority of positively buoyant plastics remain entrapped at the free surface (surface load regime) under typical flow conditions, detaching only at relatively high shear velocities. This is consistent with our surface entrapment experiments (Appendix B) and with the absorptive free-surface boundary condition used in the Lagrangian transport simulation, both shown in Figure 6**a**. For reference, the critical surface detachment parameter exceeds $\Theta_{\mathrm{cr},p,d_{50}} > 100$ for $d_{50} < 3.09$ mm, confirming that surface load is the dominant transport mode for small, buoyant plastics.

To illustrate other transport modes, we added curves of constant Rouse numbers β_p to our plot, as defined by Equation (32)

$$\frac{u_*^2}{\left(\frac{|\rho_w - \rho_p|}{\rho_w}\right) g\, d_{50}} = \left(-\sqrt{\frac{0.75\, C_2\, Re_*^2}{4\, C_1^2}} + \sqrt{\frac{0.75\, C_2\, Re_*^2}{4\, C_1^2} + \frac{Re_*}{\kappa\, C_1}\, \frac{1}{|\beta_p|}}\right)^2, \tag{32}$$

which was adopted from Pekker (2018) to account for positively and negatively buoyant plastics. Here, C_1 and C_2 are empirical coefficients that describe particle drag behaviour in the Stokes and Newton regimes, respectively, with typical values of $C_1 = 18$ and $C_2 = 0.4$ for smooth spheres (Ferguson & Church, 2004). Equation (32) was incorporated into Figure 6 to provide a more comprehensive regime classification, with typical β_p ranges for different transport modes, such as wash load, suspended load, and others, summarized in Table 1.

As discussed previously, we constructed the Surface Detachment-Rouse chart for spherical reference particles with $D_p = d_{50}$. To account for variations in particle shape and size, we relate the surface detachment parameters of an arbitrary plastic particle to those of the reference particle by expressing

$$\frac{\Theta_p}{\Theta_{p,d_{50}}} = \frac{\alpha_{p,50}}{\alpha_p} \frac{C_{D,F_w,d_{50}}}{C_{D,F_w}} \frac{\Gamma}{\Gamma_{d_{50}}}, \tag{33}$$

Table 1. Comparison of plastic transport modes for settling and rising particles with typical Shields parameter and Rouse number ranges. Transport mode thresholds are based on the Rouse-number framework of Cowger et al. (2021), with the introduction of a subsurface-load regime and Shields-based surface-detachment criteria for buoyant particles.

Transport Mode	θ_p (-), Θ_p (-)	β_p (-)	Interpretation
Settling Particles ($\beta_p > 0$)			
Bed retention	$\theta_p < \theta_{\mathrm{cr},p}$	N/A	Particles remain immobile
Bed load	$\theta_p \approx \theta_{\mathrm{cr},p}$	$\beta_p > 2.5$	Particles travel predominantly at the river bed
Suspended load	$\theta_p > \theta_{\mathrm{cr},p}$	$0.8 < \beta_p < 2.5$	Particles intermittently lifted
Wash load	$\theta_p \gg \theta_{\mathrm{cr},p}$	$0 < \beta_p < 0.8$	Turbulence keeps particles fully suspended
Rising Particles ($\beta_p < 0$)			
Wash load	$\Theta_p \gg \Theta_{\mathrm{cr},p}$	$0 < -\beta_p < 0.8$	Turbulence keeps particles fully suspended
Suspended load	$\Theta_p > \Theta_{\mathrm{cr},p}$	$0.8 < -\beta_p < 2.5$	Particles intermittently detached
Subsurface load	$\Theta_p \approx \Theta_{\mathrm{cr},p}$	$-\beta_p > 2.5$	Particles travel predominantly beneath the surface
Surface load	$\Theta_p < \Theta_{\mathrm{cr},p}$	N/A	Particles become entrapped at the surface

which leads to the following normalization of Θ_p

$$\Theta_{p,d_{50}} = \frac{\Theta_p}{\frac{\alpha_{p,50}}{\alpha_p}\frac{C_{D,F_w,d_{50}}}{C_{D,F_w}}\frac{\Gamma}{\Gamma_{d_{50}}}}. \tag{34}$$

Here, Γ and $\Gamma_{d_{50}}$ are evaluated at their respective critical submergences $(h_w/D_p)_{\mathrm{cr}}$, determined by maximising the net restoring force following Kramer (2025), such that the normalisation is consistent with the detachment curve construction. This normalization enables us to adjust the detachment parameter for plastics of varying shapes and sizes, thereby extending the regime map's applicability beyond spherical reference particles to a wide range of plastic particle geometries and dimensions.

Note that a similar approach was proposed by Goral et al. (2023); Kramer (2025) for bed entrainment, who demonstrated that the classical Shields diagram for natural sediments can be applied to plastics by expressing the plastic Shields parameter θ_p as

$$\theta_{s,d_{50}} = \frac{\theta_p}{\frac{\alpha_s}{\alpha_p}\frac{\tan(\phi_p)}{\tan(\phi_s)}\left(\frac{D_p}{d_{50}}\right)^{-0.6}}, \tag{35}$$

where the subscript s refers to sediment, and d_{50} denotes the reference sediment particle diameter $D_s = d_{50}$. The work of Kramer (2025) represents an extension of the concept proposed by Goral et al. (2023), and the form of the plastic Shields parameter is analogous to that for natural sediments, given as $\theta_p = u_*^2/\left(\left(\frac{\rho_p-\rho_w}{\rho_w}\right)gD_p\right)$, assuming $\rho_p > \rho_w$. In the context of bed entrainment, the shape factor α_p includes the projected area of the particle taken perpendicular to the flow direction. The friction coefficient ϕ accounts for particle–bed interactions: ϕ_p represents the friction coefficient between the plastic particle and the underlying sediment, while ϕ_s represents the friction between a sediment particle and the sediment bed. The corresponding Shields-Rouse diagram for negatively buoyant plastics is shown in Figure 6**b**, where the threshold for motion is given by an empirical correlation

$$\theta_{\mathrm{cr},s,d_{50}} = 0.165(Re_* + 0.6)^{-0.8} + 0.045\,\exp(-40\,Re_*^{-1.3}), \tag{36}$$

which was proposed by Sui et al. (2021). For completeness, normalized critical plastic Shields parameters $\theta_{\mathrm{cr},p}$ from Waldschläger and Schüttrumpf (2019) and (Goral et al., 2023), as re-analysed by Kramer (2025), are also included in Figure 6**b**.

In summary, this section has developed a comprehensive regime map that integrates surface detachment, bed entrainment, and the Rouse profile to classify plastic transport modes across a range of particle properties and flow conditions. By normalizing key parameters for different particle shapes and sizes, we extended classical sediment transport frameworks to plastics with varying buoyancies. The green and orange shaded areas in Figure 6 illustrate the parameter space where the Rouse profile provides a valid description of vertical plastic concentration distributions for positively and negatively buoyant particles, respectively. While the Rouse profile appears broadly applicable for negatively buoyant plastics, its applicability for positively buoyant plastics seems more limited, primarily due to the dominant influence of surface tension forces acting on small particles. This finding carries important implications for plastic surface monitoring strategies, which are further discussed in the next section. Overall, the regime map offers a valuable framework for understanding and predicting plastic transport dynamics in fluvial environments.

5.2 Limitations and Implications

While the proposed framework provides a useful basis for understanding plastic transport in fluvial systems, several limitations should be acknowledged

- **Hydrodynamic simplifications**: Our analysis does not account for waves and windage. While we anticipate that these processes are generally negligible in open-channel flows, they may be important in estuarine or coastal environments.
- **Surface boundary condition**: We applied an absorptive boundary in the Lagrangian transport simulation, corresponding to the orange shaded region in Figure 6**a**. This assumes irreversible surface entrapment and is corroborated by our experiments (Appendix B).
- **Assumed drag coefficient**: In the absence of direct measurements, we adopted a constant turbulent drag coefficient of $C_{D,F_w} = 5$. While conservative, this assumption requires experimental validation for improved accuracy.
- **Reference particle geometry**: Spherical particles were selected as a reference in the Surface Detachment–Rouse chart. This offers a reasonable first approximation, and shape effects are addressed through normalization. However, the detachment formulation may require revision for open-shaped or flexible particles, such as cups or films. As throughout the manuscript, this is a single-particle framework and does not account for particle–particle or particle–sediment interactions.
- **Effective density assumption**: Our proposed framework incorporates effective particle properties, including modified density due to processes such as fragmentation, degradation, and bio-fouling. While this provides flexibility, it assumes that such modifications are known or can be reasonably estimated. This distinction also limits direct comparison with field studies reporting positively buoyant particles distributed throughout the water column, as particles are commonly cleaned and washed prior to characterisation, such that reported densities often represent *material properties* rather than the *effective hydrodynamic properties* governing transport under field conditions.
- **Particle size effects**: The proposed framework explicitly accounts for particle-size effects through the capture-layer thickness in the development-length formulation and through the particle diameter D_p in the Surface Detachment–Rouse chart. While the

underlying concepts are expected to remain applicable across a range of particle sizes, additional validation would be beneficial.

Our findings have several important implications for understanding plastic transport in fluvial systems. Most notably, the results suggest that the applicability of classical Rouse-profile concepts to positively buoyant particles may be limited when surface-tension effects are significant. They also indicate that experimentally observed concentration profiles can be sensitive to the available development length, with measurements obtained over insufficient distances potentially reflecting transitional rather than fully developed transport conditions.

The presented Surface Detachment–Rouse chart (Figure 6**a**) highlights that the majority of positively buoyant particles are transported as surface load, suggesting that surface monitoring may be sufficient to capture the bulk of buoyant plastic transport under typical flow conditions. However, this conclusion is sensitive to hydrodynamic conditions and particle properties, as certain conditions can lead to surface detachment (Figure 6**a**). While the available evidence suggests that spherical buoyant particles are predominantly transported as surface load, further investigations are required to assess whether similar transport behaviour extends to more complex particle shapes such as films, fragments, and other irregular geometries. The apparent tension with field studies reporting positively buoyant particles distributed throughout the water column (e.g., Lenaker et al. (2019)) may partly reflect the effective-density limitation noted above. Since particles are typically cleaned and dried prior to characterisation, their reported densities may not represent the effective hydrodynamic densities governing transport under field conditions, including the effects of biofouling. Consequently, field observations of positively buoyant particles throughout the water column are not necessarily inconsistent with the proposed framework.

In addition, the developed Shields–Rouse diagram (Figure 6**b**) shows that negatively buoyant plastics are often transported as suspended load or wash load, which requires subsurface or depth-integrated sampling strategies to accurately quantify transport. Overall, our findings emphasize the importance of adapting monitoring approaches to the prevailing plastic types and local flow regimes, as a one-size-fits-all strategy may lead to substantial over- or underestimations of total plastic flux.

6 Conclusion

This study highlights the complex interactions between turbulent mixing and interfacial forces that govern the vertical distribution of buoyant plastics in open channel flows. By deriving an analytical expression for the particle development length, validated through Lagrangian simulations, we show that previous experimental investigations may not have fully met the streamwise distance required for plastics to reach an equilibrium vertical concentration profile. The introduction of a regime map integrating free surface detachment and bed entrainment processes with the modified Rouse profile provides a unified framework to predict the transport behaviour of both positively and negatively buoyant plastics. These insights are critical for improving the accuracy of plastic transport models and for designing effective sampling and mitigation strategies in riverine environments. Future work should focus on validating this framework across a range of flow conditions and particle properties to deepen our understanding of the physical processes controlling plastic transport and to refine predictive models of buoyant particle behaviour in riverine environments.

Acknowledgments

The use of the AI language model ChatGPT (OpenAI) for assistance in revising portions of the manuscript's grammar is acknowledged. All content, scientific interpretations, and conclusions remain the sole responsibility of the authors.

Notation

The following symbols are used in this paper:

Latin Symbols

A_{proj}	projected area	(m^2)
c	instantaneous plastic concentration	(kg m^{-3})
$\overline{c}$	time-averaged plastic concentration	(kg m^{-3})
c'	plastic concentration fluctuation	(kg m^{-3})
$\widehat{c}_x$	normalised vertical concentration profile at location x	(-)
$\widehat{c}_{\mathrm{ref}}$	normalised reference concentration profile	(-)
C_1, C_2	empirical coefficients describing particle drag	(-)
C_{D,F_w}	drag coefficient for downpull force	(-)
d_{50}	median grain size of underlying sediment	(m)
D_p	sphere volume-equivalent plastic diameter	(m)
D_s	sphere volume-equivalent sediment diameter	(m)
$\mathcal{D}_x$	turbulent streamwise diffusivity	(m^2 s^{-1})
$\mathcal{D}_x^*$	turbulent streamwise diffusivity at intermediate position x^*	(m^2 s^{-1})
$\mathcal{D}_z$	turbulent vertical diffusivity	(m^2 s^{-1})
$\mathcal{D}_z^*$	turbulent vertical diffusivity at intermediate position z^*	(m^2 s^{-1})
ΔC	Bray-Curtis dissimilarity metric	(-)
F_B	buoyancy force	(N)
F_W	weight force	(N)
F_w	downpull force	(N)
F_σ	surface tension force	(N)
g	gravitational acceleration	(m s^{-2})
h_w	submerged particle depth	(m)
H	water depth	(m)
L	first-passage mean development length	(m)
L_{mean}	mean particle development length	(m)
L_{95}	95th percentile particle development length	(m)
L_σ	contact length for surface tension	(m)
q	specific discharge	(m^2 s^{-1})
Re_*	shear Reynolds number	(-)
$\mathcal{R}$	random number with zero mean and unit standard deviation	(-)
t	time	(s)
T	mean first-passage time	(s)
u	instantaneous streamwise water velocity	(m s^{-1})
$\overline{u}$	time-averaged streamwise water velocity	(m s^{-1})
u'	fluctuating streamwise water velocity	(m s^{-1})
u_*	bed shear velocity	(m s^{-1})
$\mathbf{u}_p$	particle velocity vector	(m s^{-1})
U	representative horizontal advection velocity	(m s^{-1})
$\mathcal{V}_p$	particle volume	(m^3)
$\mathcal{V}_{p,w}$	submerged particle volume	(m^3)
w	instantaneous vertical water velocity	(m s^{-1})
$\overline{w}$	time-averaged vertical water velocity	(m s^{-1})
w'	fluctuating vertical water velocity	(m s^{-1})
w_s	particle settling velocity	(m s^{-1})
x	streamwise coordinate	(m)
x_p	streamwise particle position	(m)
$\mathbf{x}_p$	particle position vector	(m)
z	vertical coordinate	(m)
z_0	hydraulic roughness length	(m)

z_p	vertical particle position	(m)
z'_p	intermediate particle position for boundary condition	(m)

Greek Letters

α_p	plastic shape factor	(-)
β_p	$= w_s/(\kappa u_*)$; plastic Rouse number	(-)
β_p^*	transition Rouse number	(-)
Γ	plastic-based Bond number	(-)
Δt	simulation timestep	(s)
ε	dimensionless capture-layer thickness	(-)
ζ	dimensionless particle release elevation	(-)
η	dimensionless vertical coordinate	(-)
θ_p	plastic Shields parameter	(-)
θ_s	sediment Shields parameter	(-)
Θ_p	plastic surface detachment parameter	(-)
κ	von Kármán constant	(-)
ν_w	kinematic viscosity of water	(m^2 s^{-1})
ρ_p	plastic particle density	(kg m^{-3})
ρ_w	water density	(kg m^{-3})
σ	surface tension	(N m^{-1})
σ_L	standard deviation of $\ln(L/H)$	(-)
ϕ_p	friction coefficient between plastic and sediment bed	(-)
ϕ_s	friction coefficient between sediment particle and sediment bed	(-)
Φ	dimensionless mean first-passage time	(-)
Ψ	contact angle	(°)

Indices and Operators

bed	channel bed
cr	critical
max	maximum
p	plastic particle
ref	reference
s	sediment
source	plastic source
surf	free surface
w	water

Appendix A Asymptotic Solutions of the Mean First-Passage Equation

The dimensionless mean first-passage time $\Phi(\eta)$, Eq. (10), satisfies

$$\underbrace{\eta(1-\eta)\,\frac{\mathrm{d}^2\Phi}{\mathrm{d}\eta^2}}_{\text{diffusion}} + \underbrace{(1-2\eta)\,\frac{\mathrm{d}\Phi}{\mathrm{d}\eta}}_{\text{turbulent drift}} - \underbrace{\beta_p\,\frac{\mathrm{d}\Phi}{\mathrm{d}\eta}}_{\text{buoyant drift}} = -1, \tag{A1}$$

where $\Phi(\eta) = (\kappa u_*/H)\,T(z)$ is the dimensionless mean first-passage time and $\eta = z/H$ is the dimensionless elevation. The boundary conditions are $\frac{\mathrm{d}\Phi}{\mathrm{d}\eta}(0) = 0$ and $\Phi(1-\varepsilon) = 0$. We seek asymptotic solutions in the two limiting cases $-\beta_p \ll 1$ (turbulence-driven) and $-\beta_p \gg 1$ (buoyancy-driven).

A.1 Turbulence-Driven Regime ($-\beta_p \ll 1$)

When $|\beta_p| \ll 1$, buoyant drift is negligible relative to turbulent diffusion, and Equation (A1) reduces at leading order to

$$\eta(1-\eta)\,\frac{\mathrm{d}^2\Phi}{\mathrm{d}\eta^2} + (1-2\eta)\,\frac{\mathrm{d}\Phi}{\mathrm{d}\eta} = -1. \tag{A2}$$

The left-hand side is a perfect derivative,

$$\frac{\mathrm{d}}{\mathrm{d}\eta}\left[\eta(1-\eta)\,\frac{\mathrm{d}\Phi}{\mathrm{d}\eta}\right] = -1. \tag{A3}$$

Integrating once gives

$$\eta(1-\eta)\,\frac{\mathrm{d}\Phi}{\mathrm{d}\eta} = -\eta + C_1. \tag{A4}$$

Applying the no-flux boundary condition $\frac{\mathrm{d}\Phi}{\mathrm{d}\eta}(0) = 0$: as $\eta \to 0$ the left-hand side vanishes, so $C_1 = 0$, and

$$\frac{\mathrm{d}\Phi}{\mathrm{d}\eta} = \frac{-1}{1-\eta}. \tag{A5}$$

Integrating again,

$$\Phi(\eta) = \ln(1-\eta) + C_2. \tag{A6}$$

The absorbing boundary condition $\Phi(1-\varepsilon) = 0$ gives $C_2 = -\ln(\varepsilon)$, so

$$\Phi(\eta) = \ln\left(\frac{1-\eta}{\varepsilon}\right), \qquad -\beta_p \ll 1. \tag{A7}$$

Evaluating at the release elevation $\eta = \zeta$ recovers Equation (13). The logarithmic dependence on $(1-\zeta)/\varepsilon$ reflects the time required for diffusion to transport a particle across the remaining depth $H(1-\zeta)$ to the capture layer of thickness εH.

A.2 Buoyancy-Driven Regime ($-\beta_p \gg 1$)

When $-\beta_p \gg 1$, upward buoyant drift dominates turbulent diffusion. The diffusion operator and the turbulent-drift correction $(1-2\eta)\frac{\mathrm{d}\Phi}{\mathrm{d}\eta}$ are both subdominant and Equation (A1) reduces at leading order to

$$-\beta_p\,\frac{\mathrm{d}\Phi}{\mathrm{d}\eta} = -1, \tag{A8}$$

giving immediately

$$\frac{\mathrm{d}\Phi}{\mathrm{d}\eta} = \frac{1}{-\beta_p}. \tag{A9}$$

Integrating,

$$\Phi(\eta) = \frac{\eta}{-\beta_p} + C_3. \tag{A10}$$

Applying the absorbing boundary condition $\Phi(1-\varepsilon) = 0$ gives $C_3 = -(1-\varepsilon)/(-\beta_p)$, so

$$\Phi(\eta) = \frac{(1-\varepsilon)-\eta}{-\beta_p}, \qquad -\beta_p \gg 1. \tag{A11}$$

Evaluating at $\eta = \zeta$ recovers Equation (15). In this regime $\Phi(\zeta)$ is simply the dimensionless distance to the surface, $(1-\varepsilon-\zeta)$, divided by the dimensionless rise velocity $(-\beta_p)$, consistent with purely ballistic vertical transport.

Appendix B Surface Entrapment Experiments

A series of laboratory experiments were conducted in a 9 m long, 0.6 m wide, and 0.7 m high horizontal flume at the Hydraulics Laboratory of the University of New South Wales (Canberra). The experiments were designed to investigate the potential for particle detachment under flow conditions representative of open-channel shear over a rough bed. The channel bed was lined with a fixed layer of natural pebbles (median grain size $d_{50} = 0.02$ m) glued onto PVC sheets, providing a hydraulically rough and immobile boundary condition for all experiments.

Four experimental runs were performed using 3D-printed spherical particles with constant diameter $D_p = 0.014$ m and varying densities ρ_p, while the hydraulic forcing was systematically varied. The discharge was measured using a Promag W 400 flow meter, the median grain size of the bed material was determined via sieve analysis, and the bed shear velocity u_* was computed from particle image velocimetry (PIV) measurements of the near-bed velocity field, similar to Condo-Colcha et al. (2024). For each run, 40 particles were initially released at the channel bed, and after surfacing, their subsequent behaviour was monitored to assess whether detachment from the surface occurred.

Table B1 summarises the experimental conditions. The hydraulic forcing is characterised by unit discharge q, flow depth H, bed median grain size d_{50}, bed shear velocity u_*, and shear Reynolds number Re_*, while the particle properties are defined by diameter D_p and density ρ_p. The surface detachment parameter $\Theta_p = u_*^2/\left(\left(\frac{\rho_w-\rho_p}{\rho_w}\right) g\, D_p\right)$ was computed from measured shear velocities and particle properties, and the normalised parameter $\Theta_{p,d_{50}}$ was evaluated using Equation (34), where the Bond number ratio $\Gamma/\Gamma_{d_{50}}$ was obtained by evaluating Γ_{cr} at the critical submergence for both the experimental particle ($D_p = 0.014$ m) and the reference particle ($D_p = d_{50} = 0.02$ m), following the procedure of Kramer (2025).

Table B1. Summary of flow and particle conditions for surface entrapment experiments.

q (m^2/s)	H (m)	d_{50} (m)	u_* (m/s)	Re_*	D_p (m)	ρ_p (kg/m^3)	Θ_p	$\Theta_{p,d_{50}}$
0.1175	0.185	0.02	0.073	1457	0.014	882.5	0.33	0.24
0.1013	0.175	0.02	0.068	1350	0.014	964.7	0.95	0.52
0.1032	0.175	0.02	0.069	1375	0.014	998.0	17.36	7.03
0.0403	0.165	0.02	0.029	580	0.014	998.0	3.08	1.24

In all experimental runs, particles rose and attached to the free surface after release, and no subsequent detachment was observed. Notably, several conditions approach the surface detachment threshold in Figure 6**a**, yet surface entrapment persisted throughout, confirming the validity of the detachment curve and the dominance of the surface load regime across the tested range of flow intensities and particle densities.

Appendix C Worked Example for Surface Detachment Curve Construction

In this appendix, we provide a detailed example calculation to illustrate the procedure for constructing surface detachment curves for buoyant plastic particles in open channel flows. Using a reference particle size d_{50} and particle density ρ_p, we demonstrate how to evaluate the critical surface parameter $\Theta_{\text{cr},p,d_{50}}$ based on Equation (31). Let us assume a particle with $D_p = d_{50} = 0.005$ m and $\rho_p = 950$ kg/m^3. We further assume a drag coefficient $C_{D,F_w} = 5$, which is a conservative estimate for buoyant plastics in turbulent flow, and we consider the particle to be spherical. For a sphere, the shape factor α_p is given by the ratio of projected area times diameter to particle volume. This results in

$$\alpha_p = \frac{A_{\text{proj}} D_p}{\mathcal{V}_p} = \frac{\left(\frac{\pi}{4} D_p^2\right) D_p}{\frac{\pi}{6} D_p^3} = \frac{\frac{\pi}{4} D_p^3}{\frac{\pi}{6} D_p^3} = \frac{\frac{\pi}{4}}{\frac{\pi}{6}} = 1.5. \tag{C1}$$

Next, we consider the plastic-based Bond number, denoted as Γ_{cr}, at the point of detachment. It is defined as the ratio of the net vertical forces acting on the particle to the maximum buoyant weight difference, given by Kramer (2025)

$$\Gamma_{\text{cr}} = \frac{(F_B)_{\text{cr}} - F_W + (F_\sigma)_{\text{cr}}}{|F_{B,\max} - F_W|} = \frac{\rho_w\, g\, (\mathcal{V}_{p,w})_{\text{cr}} - \rho_p\, g\, \mathcal{V}_p + (L_\sigma)_{\text{cr}}\, \sigma \sin(\Psi)}{g\, \mathcal{V}_p\, |\rho_w - \rho_p|}. \tag{C2}$$

Here, F_B is the buoyancy force acting on the particle, F_W is the particle weight, and F_σ represents the surface tension force acting along the air-water-particle contact line. The parameters ρ_w and ρ_p are the densities of water and the particle, respectively, while g is the acceleration due to gravity. The variable $\mathcal{V}_p = \frac{\pi}{6} D_p^3 = 6.5450 \cdot 10^{-8}\,\text{m}^3$ denotes the total volume of the particle, and $(\mathcal{V}_{p,w})_{\text{cr}}$ is the critical submerged volume of the particle at detachment. The term $(L_\sigma)_{\text{cr}}$ is the critical length associated with surface tension forces, $\sigma = 0.072$ N/m is the surface tension coefficient, and $\Psi = 105°$ is the contact angle. The particle's relative submergence at detachment, that is $(h_w/D_p)_{\text{cr}}$, is given as 0.679 (Figure B1 in Kramer (2025)), so

$$h_{w,\text{cr}} = 0.679 \cdot D_p = 0.0034\,\text{m}. \tag{C3}$$

For a spherical particle, $(\mathcal{V}_{p,w})_{\text{cr}}$ and $(L_\sigma)_{\text{cr}}$ are related to $h_{\text{cr},w}$ through (Kramer, 2025)

$$(\mathcal{V}_{p,w})_{\text{cr}} = \frac{\pi\, h_{\text{cr},w}^2}{3}(1.5 D_p - h_{\text{cr},w}) = 4.9547 \cdot 10^{-8}\ \text{m}^3, \tag{C4}$$

$$(L_\sigma)_{\text{cr}} = 2\pi \sqrt{h_{\text{cr},w}\, D_p - h_{\text{cr},w}^2} = 0.0147\,\text{m}. \tag{C5}$$

Substituting these values into Equation C2 gives

$$\begin{aligned}\Gamma_{\text{cr}} &= \frac{1000 \cdot 9.81 \cdot 4.9547 \cdot 10^{-8} - 950 \cdot 9.81 \cdot 6.5450 \cdot 10^{-8} + 0.0147 \cdot 0.072 \cdot \sin(105°)}{9.81 \cdot 6.5450 \cdot 10^{-8} \cdot (1000 - 950)} \\ &= 27.9141.\end{aligned} \tag{C6}$$

This result is then used in Equation (31) to compute the critical surface detachment parameter

$$\Theta_{\text{cr},p,d_{50}} = \frac{u_{*,\text{cr}}^2}{\left(\frac{\rho_w - \rho_p}{\rho_w}\right) g\, D_p} = \frac{9.17\, \Gamma_{\text{cr}}}{\alpha_p\, C_{D,F_w}} = \frac{9.17 \cdot 27.9141}{1.5 \cdot 5} = 34.1297. \tag{C7}$$

The critical shear velocity is

$$\begin{aligned}u_{*,\text{cr}} &= \left(\Theta_{\text{cr},p,d_{50}} \left(\frac{\rho_w - \rho_p}{\rho_w}\right) g D_p\right)^{0.5} \\ &= \left(34.1297 \cdot \left(\frac{1000 - 950}{1000}\right) \cdot 9.81 \cdot 0.005\right)^{0.5} = 0.2893\,\text{m/s},\end{aligned} \tag{C8}$$

which corresponds to a shear Reynolds number of

$$Re_* = \frac{u_*\, d_{50}}{\nu_w} = \frac{0.2893 \cdot 0.005}{1 \cdot 10^{-6}} = 1446.6. \tag{C9}$$

The calculated pair of critical values, $Re_* = 1446.6$ and $\Theta_{\text{cr},p,d_{50}} = 34.13$, characterizes the onset of particle detachment for the given buoyant plastic particle under the specified flow conditions (Figure 6**a**).

References

Alsina, J. M., Jongedijk, C. E., & van Sebille, E. (2020). Laboratory measurements of the wave-induced motion of plastic particles: influence of wave period, plastic size and plastic density. *Journal of Geophysical Research: Oceans*, *125*(12), e2020JC016294.

Born, M. P., Bruell, C., Schaefer, D., Hillebrand, G., & Schuettrumpf, H. (2023). Determination of microplastics' vertical concentration transport (rouse) profiles in flumes. *Environmental Science & Technology*, *57*(14), 5569–5579.

Bray, J. R., & Curtis, J. T. (1957). An ordination of the upland forest communities of southern wisconsin. *Ecological Monographs*, *27*(4), 325–349. doi: 10.2307/1942268

Claudin, P., Charru, F., & Andreotti, B. (2011). Transport relaxation time and length scales in turbulent suspensions. *Journal of Fluid Mechanics*, *671*, 491–506.

Condo-Colcha, F., Niven, R., & Kramer, M. (2024, December 1). *Effects of aspect ratio on the incipient motion of plastics in open-channel flows.* AFMC2024, Canberra, Australia. Retrieved from `https://doi.org/10.5281/zenodo.14213323` (Licensed under CC BY 4.0) doi: 10.5281/zenodo.14213323

Cowger, W., Gray, A. B., Guilinger, J. J., Fong, B., & Waldschläger, K. (2021). Concentration depth profiles of microplastic particles in river flow and implications for surface sampling. *Environmental Science & Technology*, *55*(9), 6032–6041.

Dey, S. (2014). *Fluvial hydrodynamics.* Springer.

Ferguson, R., & Church, M. (2004). A simple universal equation for grain settling velocity. *Journal of sedimentary Research*, *74*(6), 933–937.

Gardiner, C. W. (1985). *Handbook of stochastic methods for physics, chemistry and the natural sciences* (2nd ed.). Berlin: Springer.

Gent, M. R., Menendez, M., Toraño, J., Isidro, D., & Torno, S. (2009). Cylinder cyclone (larcodems) density media separation of plastic wastes. *Waste Management*, *29*(6), 1819–1827.

Goral, K. D., Guler, H. G., Larsen, B. E., Carstensen, S., Christensen, E. D., Kerpen, N. B., … Fuhrman, D. R. (2023, June). Shields Diagram and the Incipient Motion of Microplastic Particles. *Environmental Science & Technology*, *57*(25), 9362–9375. Retrieved 2026-04-03, from `https://pubs.acs.org/doi/10.1021/acs.est.3c02027` doi: 10.1021/acs.est.3c02027

Gräwe, U., Deleersnijder, E., Shah, S. H. A. M., & Heemink, A. W. (2012). Why the euler scheme in particle tracking is not enough: the shallow-sea pycnocline test case. *Ocean Dynamics*, *62*, 501–514.

Grigorescu, R. M., Grigore, M. E., Iancu, L., Ghioca, P., & Ion, R.-M. (2019). Waste electrical and electronic equipment: A review on the identification methods for polymeric materials. *Recycling*, *4*(3), 32.

Kramer, M. (2025). Surface detachment and bed entrainment of fluvial plastics. *Water Resources Research*, *61*(9).

Lenaker, P. L., Baldwin, A. K., Corsi, S. R., Mason, S. A., Reneau, P. C., & Scott, J. W. (2019). Vertical distribution of microplastics in the water column and surficial sediment from the milwaukee river basin to lake michigan. *Environmental Science & Technology*, *53*(21), 12227–12237. doi: 10.1021/acs.est.9b03850

Mark, J. E. (2009). Polymer data handbook.

Nezu, I., & Nakagawa, H. (1993). *Turbulence in open-channel flows.* Rotterdam: Balkema.

Nordam, T., Kristiansen, R., Nepstad, R., & Röhrs, J. (2019). Numerical analysis of boundary conditions in a lagrangian particle model for vertical mixing, transport and surfacing of buoyant particles in the water column. *Ocean Modelling*, *136*, 107–119.

Nordam, T., Kristiansen, R., Nepstad, R., van Sebille, E., & Booth, A. M. (2023). A comparison of Eulerian and Lagrangian methods for vertical particle transport in the water column. *Geoscientific Model Development Discussions*, *2023*, 1–41.

Pekker, L. (2018). Particle transport in microchannels. *Journal of Imaging Science and Technology*, *62*(4), 040408-1–040408-6. doi: 10.2352/J.ImagingSci.Technol.2018.62.4.040408

Rossman, L. A., & Boulos, P. F. (1996). Numerical methods for modeling water quality in distribution systems: A comparison. *Journal of Water Resources planning and management*, *122*(2), 137–146.
Rouse, H. (1937). Modern conceptions of the mechanics of fluid turbulence. *Transactions of the American Society of Civil Engineers*, *102*(1), 463–505.
Sui, T., Staunstrup, L. H., Carstensen, S., & Fuhrman, D. R. (2021). Span shoulder migration in three-dimensional current-induced scour beneath submerged pipelines. *Coast. Engng.*, *164*.
Valero, D., Belay, B. S., Moreno-Rodenas, A., Kramer, M., & Franca, M. J. (2022). The key role of surface tension in the transport and quantification of plastic pollution in rivers. *Water research*, *226*, 119078.
Visser, A. W. (1997). Using random walk models to simulate the vertical distribution of particles in a turbulent water column. *Marine Ecology Progress Series*, *158*, 275–281.
Waldschläger, K., & Schüttrumpf, H. (2019). Erosion behavior of different microplastic particles in comparison to natural sediments. *Environ. Sci. Technol.*, *53*(22), 13219-13227. doi: https://pubs.acs.org/doi/abs/10.1021/acs.est.9b05394
Wickramarachchi, C., Niven, R., & Kramer, M. (2024). Numerical plastic transport modelling in fluvial systems: Review and formulation of boundary conditions. *Water Research*, 122947.
Wright, K., Hariharan, J., Passalacqua, P., Salter, G., & Lamb, M. P. (2022). From grains to plastics: Modeling nourishment patterns and hydraulic sorting of fluvially transported materials in deltas. *Journal of Geophysical Research: Earth Surface*, *127*(11).
Zaat, L. (2020). *Below the surface: A laboratorial research to the vertical distribution of buoyant plastics in rivers* (Master's Thesis). Delft University of Technology.